

EFFECT OF SOLIDIFICATION PARAMETERS ON THE MICROSTRUCTURE AND TENSILE PROPERTIES OF 319-TYPE ALLOYS

A. M. Samuel and F. H. Samuel

Département des Sciences appliquées, Université du Québec à Chicoutimi, Chicoutimi, QC, Canada

H. W. Doty

General Motors Materials Engineering, Pontiac, MI, USA

Salvador Valtierra

Nemak, S.A., Garza Garcia, N.L., Mexico

Copyright © 2016 American Foundry Society
DOI 10.1007/s40962-016-0110-y

Abstract

The present study was performed on an Al–Si–Cu 319-type alloy using an end-chill mold, while varying the cooling rate along the solidification axis. Good fits for response parameters of percent porosity, maximum pore area, average pore area, maximum pore length and average pore length were obtained from the statistical analysis of the porosity data for the end-chill mold samples. These results strongly support the porosity formation observed in an aluminum A319.2 alloy reported in an earlier study. Tensile samples were T6-heat-treated, and the data obtained from these samples were analyzed statistically. The results show that the ultimate tensile strength (UTS) is sensitive to variations in the porosity and solidification conditions, and varies in a nonlinear fashion with respect to both, while the yield strength is practically unaffected. Ductility is also

sensitive to variations in porosity and cooling rate, following a trend similar to that shown by the UTS. Increasing the porosity volume fraction above 0.5 % in the base alloy (unmodified and non-grain-refined) reduces the ductility to negligible levels. Strontium modification and grain refining allow for increases in porosity before the same level of degradation in ductility is observed. The cooling rate significantly influences the ductility at low hydrogen levels. At higher levels, however, hydrogen has a more pronounced effect (porosity related) on the drop in ductility.

Keywords: aluminum alloys, porosity, modification, grain refining, tensile properties, statistical analysis

Introduction

Two important factors that determine the eventual quality and properties of aluminum cast components are the solidification rate and porosity. Solidification rate affects the microstructure, as well as the porosity formed, while porosity affects the surface quality, soundness, corrosion resistance and other properties. Apart from solidification rate, microstructural control is also achieved through grain refinement and modification, where small additions of Al–Ti–B and Al–Sr master alloys, respectively, provide the means for producing refined microstructures and the required morphology of constituent phases.^{1–7}

With regard to porosity, its formation is attributed mainly to two effects: (1) shrinkage, resulting from the volume decrease accompanying solidification, and (2) the evolution of dissolved gases, resulting from the decrease in solubility of these gases in the solid, as compared to the liquid metal. Hydrogen, the only gas capable of dissolving to a significant extent in molten aluminum but exhibiting very low solubility in the solid state, is mainly responsible for the gas porosity in the casting, together with the pressure during solidification, the chemical composition and solidification range of the alloy, and the solidification rate. Shrinkage porosity can also occur as “microshrinkage” or “microporosity,” dispersed in the interstices of dendritic

solidification regions. Limited or inadequate liquid metal feeding in the dendritic solidification area gives rise to this type of porosity.^{8–10}

Grain refining, modification and the inclusion content of the melt also influence porosity formation. Melt cleanliness, with particular regard to the presence of oxides and inclusions, is recognized as an important factor that influences hydrogen gas nucleation.¹¹ More often than not, the various factors contributing to porosity manifest themselves simultaneously, interacting with each other to develop the resulting porosity observed.

Although porosity in aluminum alloys has been investigated, detailed systematic data on different alloy systems in terms of parametric studies of the porosity formation and distribution are generally not available. In the case of the cast aluminum alloy 319, it ranks as one of the commercially important alloys used in automotive applications on account of its excellent casting characteristics and good mechanical properties, for instance, relatively little is to be found in the literature on such studies, as compared to the A356 automotive alloy.^{12,13} In fact, studies reported by our group^{14–17} appear to be among the few that cover porosity formation in Al–Si–Cu–Mg alloys, compared to numerous investigations carried out on Al–Si cast alloys.

This lack of design data, particularly in the know-how of controlling the formation of porosity and its effect on secondary properties (e.g., fatigue, wear and corrosion) in these alloys, poses constraints on their applicability. Addressing this issue by providing such data would certainly remedy the situation. The aim of the present project, therefore, was to distinguish the different factors affecting porosity and to determine their individual and combined effects on porosity formation in 319 alloy, in relation to the product quality, the systematic data generated from the work to be used to obtain a response surface model of the porosity behavior of this alloy.

The present work was undertaken to:

1. Study the effect of hydrogen content (0.1–0.4 ml/100 g Al), modification (Sr: 0–300 ppm) and grain refinement (TiB₂: 0–0.02 wt%) on the porosity formation and distribution in 319 commercial aluminum alloy.
2. Carry out a parametric study of the evolution of porosity in the Al–Si–Cu–Mg system in order to develop a response surface model of the porosity behavior of this alloy system as a function of alloy and process parameters.
3. Obtain a correlation between porosity and tensile properties: yield strength (YS), ultimate tensile strength (UTS) and ductility or fracture elongation (El. %).

Experimental Procedure

The A319.2 aluminum alloy used in this study was supplied in the form of 12.5-kg ingots. The chemical composition of the as-received alloy is shown in Table 1. The ingots were melted in a silicon carbide crucible of 7-kg capacity, using an electric resistance furnace. The melting temperature was held at 735 ± 5 °C. At this temperature, the molten metal was either degassed using high-purity argon (melt hydrogen content ~ 0.1 ml/100 g Al—designated H1) or gassed (melt hydrogen content 0.2–0.24 ml/100 g Al—designated H2 or ~ 0.32 – 0.36 ml/100 g Al—designated H3). Melts were also modified with strontium (with Sr levels of ~ 70 – 90 ppm—designated S1, 120–180 ppm—designated S2, 250–310 ppm—designated S3) using Al–10 wt% Sr master alloy and grain-refined by means of Al–5 wt% Ti–1 wt% B master alloy to obtain a 0.02 wt% Ti content (designated T). The melt hydrogen level was monitored using an AlScan™ unit and was also determined from “Ransley” samples obtained from Ransley mold castings of each melt, using the Leco vacuum fusion technique.¹⁸ For each pouring, samplings for chemical analysis were also taken. The samples were analyzed using inductive plasma couple (ICP) or spectrometric analysis elsewhere.

Casting was carried out using a rectangle-shaped end-chill mold made of refractory material (to ensure directional solidification and good thermal insulation), where the molten metal was poured through 8 pores/cm (i.e., 20 ppi) ceramic foam filter disks fitted into the riser (above the sprue) to avoid incident inclusions. Figure 1a shows a schematic diagram of the end-chill mold, the chill consisting of a copper box at the bottom through which cold water was circulated. Prior to casting, the mold was preheated to 150 °C/302 °F to drive out moisture. The water was turned on the moment the liquid metal had half-filled the mold. To reduce heat loss from the open surface, the top of the end-chill mold was covered with an insulated ceramic board as soon as the mold was completely filled. Figure 1b reveals the temperature–time curves along the solidification direction.

Such a casting arrangement produced ingots with solidification rates which decreased with increasing distance from the chill. Obtained ingot dimensions were approximately 7 cm × 14 cm × 20 cm. Table 2 indicates the average secondary dendrite arm spacings (SDAS) and local cooling rates that were obtained (from the respective microstructures and thermal analysis cooling curves), corresponding to different distances from the chill end.

The number of castings representing all the conditions studied was 24 in all, covering the H, HS, HT and HTS series, with H and S further divided as H1, H2 and H3, and S1, S2 and S3 according to the 3 levels of hydrogen or strontium selected for a particular casting (H, S and T denoting the hydrogen, strontium and grain refiner levels of the melt from which the casting was obtained). Table 3

Table 1. Chemical Composition of the A319.2 Alloy (wt%)

Element (wt%)								
Si	Cu	Fe	Mn	Mg	Ti	Sr	Zn	Ni
6.23	3.77	0.46	0.14	0.06	0.073	0.0003	0.08	0.008

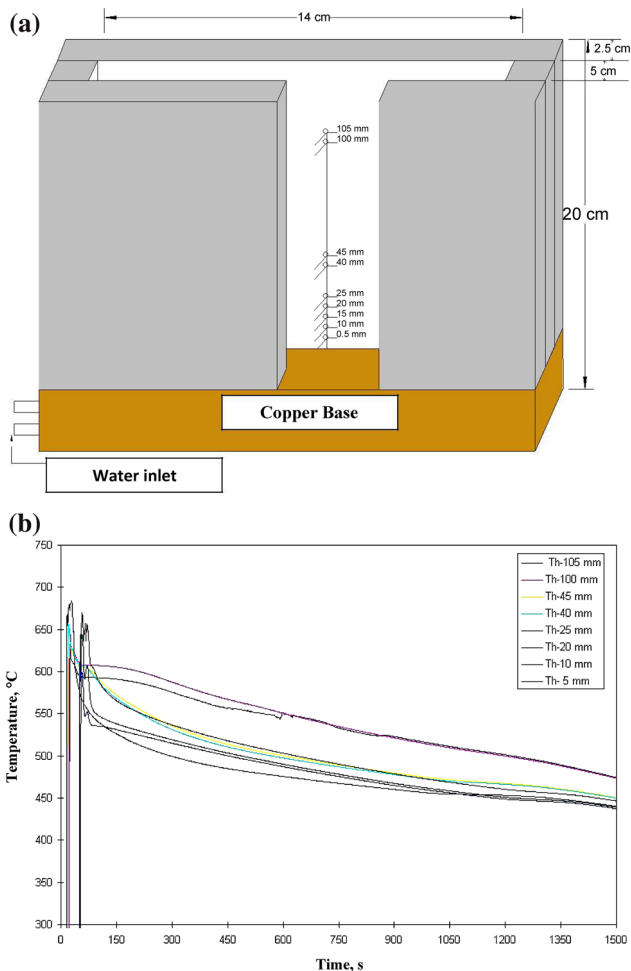


Figure 1. (a) Directional solidification mold. (b) Temperature–time curves obtained from the end-chill mold along the solidification direction—non-modified alloys.

enumerates the different castings that were produced. For each condition, three identical castings were made: one for microstructural analysis and porosity measurements, and two for tensile property measurements. Samples were sectioned from the cast blocks in the horizontal orientation at varying heights (5, 10, 20, 40 and 100 mm) above the water-chilled copper base, from which metallographic or tensile test sheet specimens were prepared for metallographic observations or tensile testing purposes, respectively. Table 4 lists the actual chemical compositions.

Five samples (2 cm × 3 cm) from each end-chill casting were obtained and cut from the central portion of the

Table 2. Variation in Secondary Dendrite Arm Spacing as a Function of Distance from the Chill End in an End-Chill Casting

Distance from chill end (mm)	Average SDAS (μm)
5	15
10	28
20	52
40	73
100	95

casting at the five levels of 5, 10, 20, 40 and 100 mm above the end-chill bottom, as mentioned previously. Microstructural changes on polished surfaces of these metallographic samples were examined using optical microscopy. The α-aluminum SDAS, eutectic Si and β-iron Al₅FeSi phase particle characteristics and the porosity were analyzed/quantified using a Clemex image analyzer in conjunction with the optical microscope (Olympus PMG3).

Corresponding to the 24 end-chill castings listed in Table 3, a total of 120 metallographic samples (24 castings × 5 levels) were obtained for which porosity measurements were carried out using image analysis (Clemex image analyzer in conjunction with an Olympus PMG3 optical microscope). For these measurements, the number of fields (“field” representing the field of view of the optical microscope and covering an area of $2.23 \times 10^6 \mu\text{m}^2$ at 50× magnification) examined is chosen so as to cover the entire area of the specimen. That is to say, the entire surface of the specimen is traversed in a regular, systematic fashion and the porosity (or other particle/phase) characteristics noted for the selected number of fields. In the present case, one hundred fields were required at 50× magnification to cover the entire sample surface area. The parameters measured were the area percent porosity (i.e., porosity % measured over a constant sample surface area), pore area, pore length and pore aspect ratio, as well as the pore count.

Sheet samples for tensile testing (60 mm × 20 mm × 3 mm) were obtained from each end-chill casting at the same five levels of 5, 10, 20, 40 and 100 mm above the chill end, with the samples being cut in such a way that their centerlines passed through the five levels. The samples were heat-treated at 180 °C/8 h, air-cooled and

Table 3. List of End-Chill Castings Prepared in the Present Work

Series	Castings	Series	Castings
H	H1, H2, H3	HT	H1T, H2T, H3T
HS	H1S1, H2S1, H3S1	HTS	H1TS1, H2TS1, H3TS1
	H1S2, H2S2, H3S2		H1TS2, H2TS2, H3TS2
	H1S3, H2S3, H3S3		H1TS3, H2TS3, H3TS3

Table 4. Chemical Composition of Alloys Used in Directional Solidification

Alloy codes	Si (%)	Cu (%)	Zn (%)	Fe (%)	Mg (%)	Mn (%)	Ti (%)	Sr (%)	Gr (%)	H (ml/100 g)
H1	5.80	3.80	0.072	0.47	0.01	0.079	0.077	<0.001	0	0.10
H1S1	5.67	2.81	0.077	0.42	0.039	0.067	0.065	0.018	0	0.10
H1S2	6.26	2.98	0.097	0.45	0.038	0.074	0.070	0.018	0	0.10
H1S3	5.76	3.23	0.071	0.47	0.013	0.078	0.075	0.032	0	0.10
H1S1T	5.97	3.29	0.078	0.42	0.014	0.077	0.086	0.009	0.02	0.10
H1S2T	5.97	3.37	0.072	0.47	0.013	0.079	0.088	0.015	0.02	0.10
H1S3T	6.43	3.04	0.066	0.44	0.013	0.071	0.082	0.025	0.02	0.10
H1T	5.81	3.19	0.070	0.45	0.032	0.075	0.091	0.002	0.02	0.10
H2	6.25	3.71	0.083	0.46	0.052	0.13	0.13	<0.001	0	0.22
H2S1	6.23	3.77	0.080	0.46	0.060	0.14	0.073	0.01	0	0.19
H2S2	6.23	3.77	0.080	0.46	0.060	0.14	0.073	0.021	0	0.21
H2S3	6.36	3.74	0.085	0.48	0.050	0.13	0.14	0.025	0	0.25
H2S1T	6.23	3.77	0.080	0.46	0.060	0.14	0.17	0.004	0.02	0.23
H2S2T	6.23	3.77	0.080	0.46	0.060	0.14	0.12	0.011	0.02	0.26
H2S3T	6.23	3.96	0.070	0.511	0.049	0.14	0.148	0.024	0.02	0.24
H2T	6.36	3.76	0.084	0.48	0.051	0.13	0.16	0.013	0.02	0.19
H3	6.24	3.74	0.082	0.47	0.048	0.13	0.073	0.0001	0	0.35
H3S1	6.23	3.77	0.080	0.46	0.060	0.14	0.073	0.009	0	0.33
H3S2	6.23	3.77	0.080	0.46	0.060	0.14	0.073	0.017	0	0.29
H3S3	6.26	3.74	0.082	0.47	0.046	0.13	0.14	0.029	0	0.35
H3S1T	6.23	3.77	0.080	0.46	0.060	0.14	0.16	0.007	0.02	0.35
H3S2T	6.23	3.77	0.080	0.46	0.060	0.14	0.12	0.009	0.02	0.35
H3S3T	6.22	3.73	0.082	0.047	0.049	0.13	0.19	0.027	0.02	0.34
H3T	6.22	3.73	0.082	0.47	0.050	0.13	0.16	0.0005	0.02	0.30

tensile-tested at room temperature using an MTS servo-hydraulic machine at a strain rate of 4×10^{-4} /s. Tensile properties, i.e. yield strength at 0.2 % offset strain, UTS and fracture elongation were derived from the data acquisition system attached to the testing machine.

Samples for SEM examination were sectioned from the tensile-tested specimens about 1 cm below the fracture surface and were then mounted with care for fracture surface examination. The fracture surface for each of the tested specimens was examined using a JEOL 840A scanning electron microscope operating at 15 kV and 3A.

Results and Discussion

Microstructural Characterization and Statistical Analysis

Earlier studies^{19–22} have shown that β -Al₅FeSi phase platelets are very active as pore nucleation sites, in that small pores are often found nucleated along the long sides of the platelets. Such a mechanism is expected to result in an increase in pore density, which is strongly related to the metal feedability or the ease with which the molten metal can flow into the different sections of the casting mold.

However, in spite of the harmful effect of the β -platelets as pore nucleation sites, their presence seems to limit pore growth. Figure 2 shows how the β -platelets limit the lateral growth of both gas and shrinkage pores. Proper control of this phase thus becomes important from both properties and porosity points of view. Essential features observed with respect to the occurrence of the β - Al_5FeSi phase in the current study are as follows:

1. The SDAS critically affects the size of the β -platelets, the latter being indicative of the volume fraction of the phase obtained in the sample. Figure 3 compares the microstructures of H1 alloy samples (degassed alloy, no melt treatment) obtained at 5 mm and 100 mm levels above the chill end showing how they are extremely difficult to discern at the highest cooling rate, but are observed in relative abundance at the slow cooling rate of the 100 mm (above the chill end) sample.
2. In the unmodified alloy (H1), sympathetic (preferential) nucleation of the platelets is observed, leading to the branching of several platelets from a parent needle. Addition of Sr is seen to reduce this effect, the Sr poisoning the nucleation sites and assisting in the dissolution of the β -platelets. An addition of 300 ppm Sr (H1S3 alloy) is seen to accelerate the dissolution process, leading to the fragmentation of the platelets into smaller segments (cf. 60–80 μm with 120–1200 μm in the untreated H1 alloy).
3. A tendency for thickening of the β -platelets is observed with grain refining, along with the sympathetic nucleation/branching effect noted in the untreated alloy. The thickening takes place via a step-like motion of ledges as shown in Figure 4. Brittle fracture of thick platelets was observed to occur, different from the fragmentation that occurs due to Sr modification.

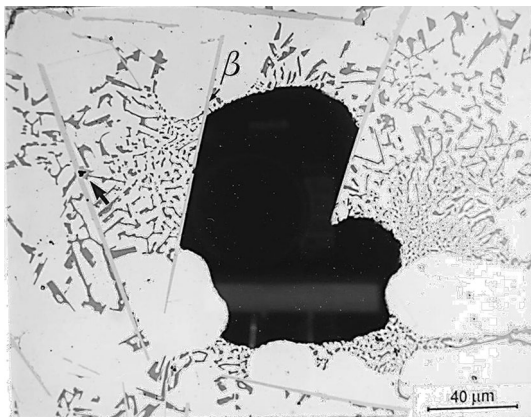


Figure 2. Role of β - Al_5FeSi platelets in restricting the growth of gas porosity. Note the presence of small pores along the long sides of the β -platelets (arrowed).

4. A comparison of the β -platelet densities for H1, H1T, H1S3 and H1TS3 alloys at the 100 mm level (SDAS $\sim 90 \mu\text{m}$) reveals that the H1S3 alloy sample gives the lowest platelet density (Figure 5).

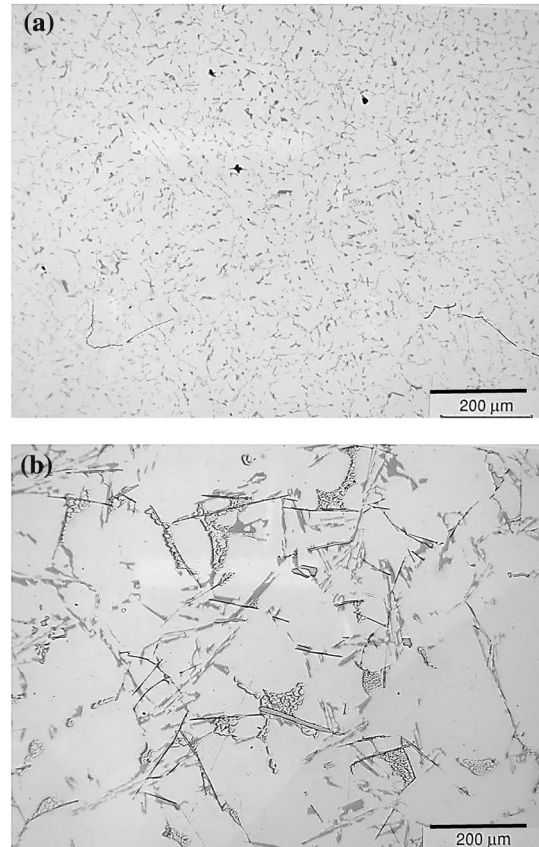


Figure 3. Microstructures of H1 alloy samples obtained at: (a) 5 mm, (b) 100 mm levels above the chill end showing the relative abundance of β - Al_5FeSi platelets in the latter case.

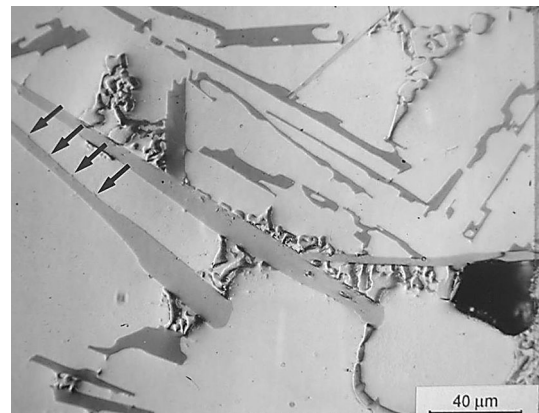


Figure 4. Microstructure of H1T alloy at 100-mm distance above the chill, showing thickening of the β - Al_5FeSi needle via a step-like motion of ledges (arrowed).

- Use of a grain refiner decreases the beneficial effect obtained with Sr addition.

The microstructure of H1 alloy at 5-mm distance from the chill showed very small and well-scattered pores. At 100-mm distance from the chill, pores were seen in the

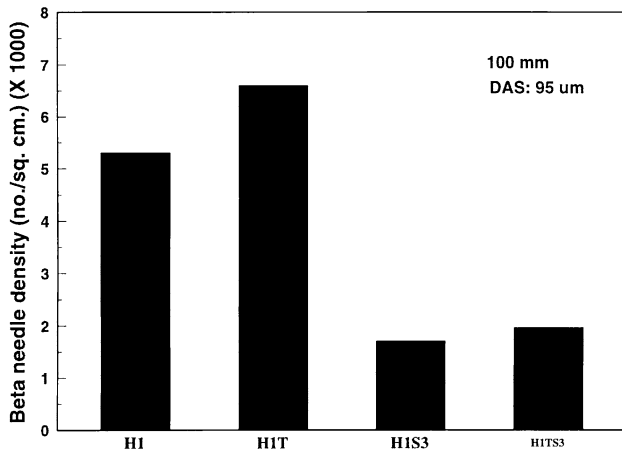


Figure 5. Histogram comparing the β -platelet densities of H1 alloys at 100-mm distance from the chill end.

interdendritic regions and disconnected, and their lengths were approximately the same as the dendrite arms or even less, as shown in Figure 6a. The microstructure of H1S3 alloy at 5-mm distance from the chill, Figure 6b did not reveal much change in porosity size and distribution above what was observed in the corresponding H1 sample. However, the structure changed dramatically as the distance from the chill increased to 100 mm (Figure 6c). The pores were rounded, and an increase in pore size and percentage porosity was observed.

In the grain-refined alloy (HIT), a well-dispersed distribution of small pores was observed, with the pores occurring either at the grain boundaries or within the grains. The variation in percentage porosity with SDAS for degassed and filtered melt castings of the H1 alloys under different melt treatment conditions is summarized in Figure 7. It is well established that hydrogen is the strongest determinant of all the parameters that contribute to porosity formation. This was clearly evidenced from the microstructures of the H3 alloy samples. At a 5-mm distance from the chill, two distinct pore morphologies, elongated and rounded, could be observed, as shown in Figure 8a. At a 100-mm distance, however, the majority

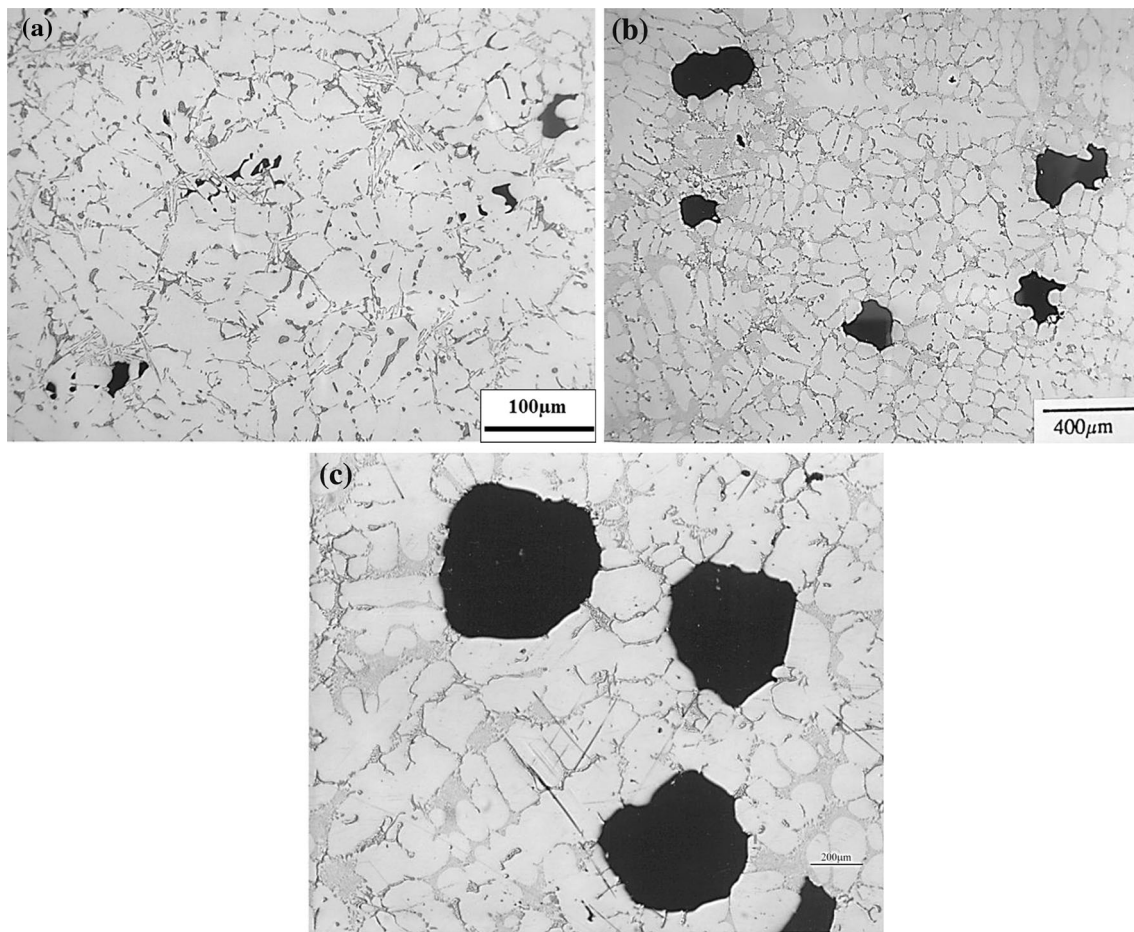


Figure 6. Microstructures showing porosity distribution in: (a) H1 alloy at 5 mm, (b) H1S3 alloy at 5 mm, (c) H1S3 alloy at 100-mm distance above the chill.

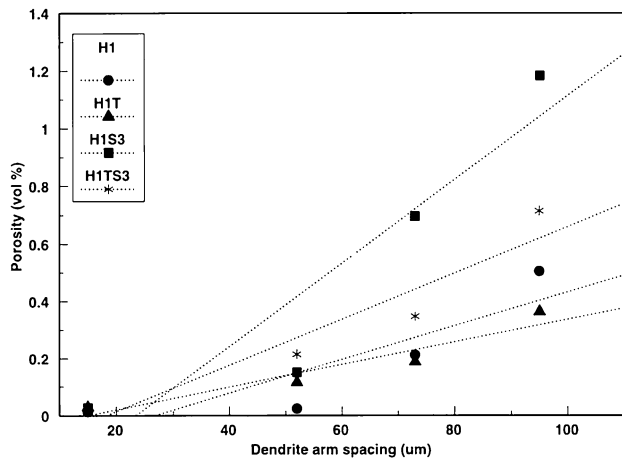


Figure 7. Variation in percentage porosity with SDAS for H1 alloys.

of pores were rounded, as shown in Figure 8b. The hydrogen–strontium interaction effect on porosity (H3S3 alloy) resulted in pores that were mostly round as opposed to the mixture of rounded and elongated forms observed in the case of H3 alloy (at a 5-mm distance from the chill). This treatment was also associated with an increase in the area pore density. A decrease in the cooling rate (i.e., at 100 mm above the chill) resulted in pores that were larger and more spherical than those observed in H3 alloy.

Samples obtained from the H3TS3 alloy and etched in Keller’s reagent were examined to determine the nucleation mechanism of pores. At low cooling rates (5-mm distance from the chill), the pores (elongated or rounded) were mostly found nucleated at or along the grain boundaries. At intermediate cooling rates (20-mm distance from the chill), while most of the pores were nucleated in the intergranular regions, some were observed in the interdendritic regions, as shown in Figure 9 (thick white arrow shows the presence of TiB_2 in the interior of the pores). At the highest cooling rate (100-mm distance from the chill) also, the possibility of pore nucleation in the intergranular regions was still evident.

Porosity formation and growth in aluminum alloy castings has been extensively investigated, both experimentally and theoretically, using mathematical modeling (refer to the works listed in the two overviews in Reference 7). In order to link the two, statistical analysis using data reduction techniques is one of the more recent means increasingly being applied to quantitatively predict porosity formation in such alloy castings, based on the results obtained from a planned set of experiments (variously termed factorial or fractional factorial designs^{14,18} according to the designed input), where the response parameters (those of porosity) can be quantitatively related to the predictor or controlling parameters

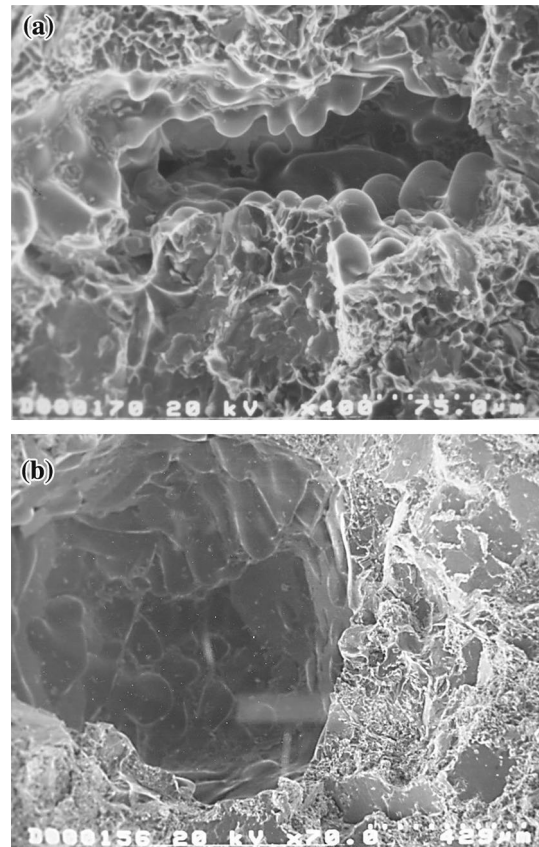


Figure 8. Microstructures of (a) H3 alloy at 5 mm, (b) H3 alloy at 100 mm.

determined by the alloying and melt conditions set by the experiments.

Such statistically designed experiments are very efficient in that they provide a fixed amount of information with much less effort than the classic approach using one variable at a time would demand. More importantly, they provide information about the interactions between the controlling variables, which constitutes a very significant factor in the search of optimum conditions, in this case, that of obtaining quality castings containing minimum porosity. The effectiveness of this approach—termed response surface methodology—has been variously demonstrated in the case of an A356 alloy by Tynelius et al.⁷ and in Al–Si–Cu–X alloys by Roy¹⁸ and Roy et al.²³

Apart from presenting the results in a simple manner and extracting the maximum information possible from a given set of experiments, statistical methods can also aid the experimenter to arrive at the correct conclusions in spite of variability in the experimental results.¹⁵ Among the different analytical methods available, that of multiple regression analysis, using stepwise reduction, was selected, for the above-mentioned reasons, namely the ability of this technique to detect and evaluate the interactive effects of

the several predictor parameters on the response parameters.

As previously mentioned, the porosity data obtained for the 135 end-chill samples were further analyzed to obtain (1) pore density versus pore area and (2) pore density versus pore length distributions, from which the average and maximum pore area/pore length values and respective pore densities were determined for the two parts of the distribution curves representing small and large pores. The area percent porosity was also determined in each case. These values constitute the *response* parameters that are obtained as a result of the alloy parameters (chemical composition) and thermal parameters (cooling rate and solidus velocity) of each sample (viz. the predictor or controlling parameters). The final data set comprising all of these parameters was analyzed using multiple regression analysis, to derive contour plots to predict the effect (independent and/or

interactive) of the various predictor parameters on the porosity.

It is not within the scope of the present study to go into the details of the procedures and various tests conducted in such an analysis; these are well covered in standard text books such as those of Box et al.,²⁴ Davies²⁵ and Casella.²⁶ Essentially, for any statistical analysis, the four essentials required are: (1) the experimental data collection (results) or population, (2) the mean value of these results, (3) a quantitative means of representing the results, e.g., by the standard deviation or variance and (4) the means to assess the validity of the results/conclusions, using a test of significance. Such a test gives the probability that the difference between a sample value and a hypothesized value is due only to sampling error. For a sample value to be statistically significant, this difference must be low. The mean and standard deviation (or variance) enables us to indicate the precision with which we can state the characteristics of the population or data collection by quoting confidence intervals or limits within which the true value very probably lies.²⁴

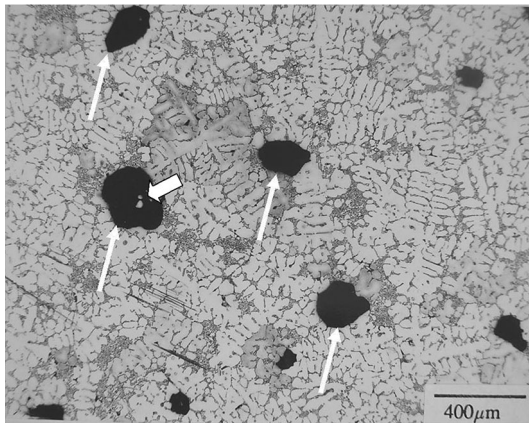


Figure 9. Microstructure obtained from H3TS3 alloy and etched in Keller's reagent. Note the presence of porosity at the grain boundaries—arrowed.

The multiple regression analysis of the porosity data obtained in the present study was carried out using StatSoft Statistica, a comprehensive, integrated statistical data analysis, graphic and database management system featuring a wide selection of basic and advanced analytical procedures including a multiple regression module. The latter program, covering a vast range of regression techniques including simple, multiple, stepwise, nonlinear (polynomial, exponential, log, etc.) and Ridge regression, is capable of calculating a comprehensive set of statistics including the complete regression table.

A forecasting routine allows the user to perform “what-if” analyses and to interactively compute predicted scores based on user-defined values of predictors. Extremely large

Table 5. Response Surface Models Obtained for Porosity Behavior in End-Chill Cast Samples

Response parameter (model)	Predictor variables used in model (<i>t</i> values and significance levels given below each)							R^2 value
	H	SDAS	Sr	Ti	Mg	Cu	TS	
Percentage porosity	9.470	7.902	6.564	-2.910	3.674	3.112	-2.078	0.832
	0.00000	0.00000	0.00000	0.00426	0.00035	0.00228	0.03969	
Maximum pore area (μm^2)	8.721	22.350	4.782	-3.684	8.403			0.873
	0.00000	0.00000	0.000005	0.00033	0.00000			
Average pore area (μm^2)	6.125	11.085	7.0599	-3.838	5.316	2.494	-2.821	0.831
	0.00000	0.00000	0.00000	0.00019	0.00000	0.01388	0.00555	
Maximum pore length (μm)	6.061	7.110	4.682	-5.458	6.346		3.376	0.812
	0.00000	0.00000	0.000007	0.00000	0.00000		0.00097	
Average pore length (μm)	5.333	16.639	3.478	-5.145	5.167			0.768
	0.00000	0.00000	0.000687	0.000001	0.000001			

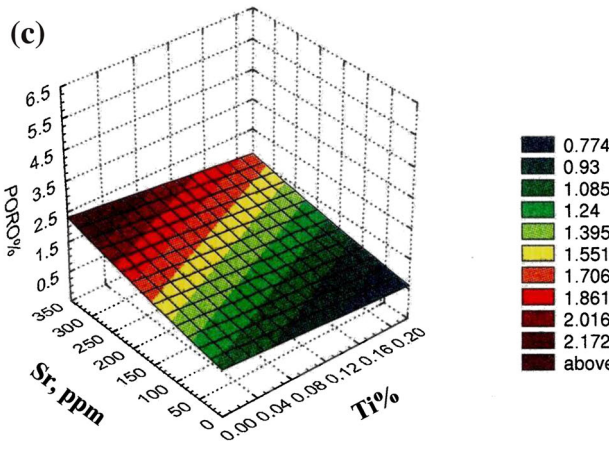
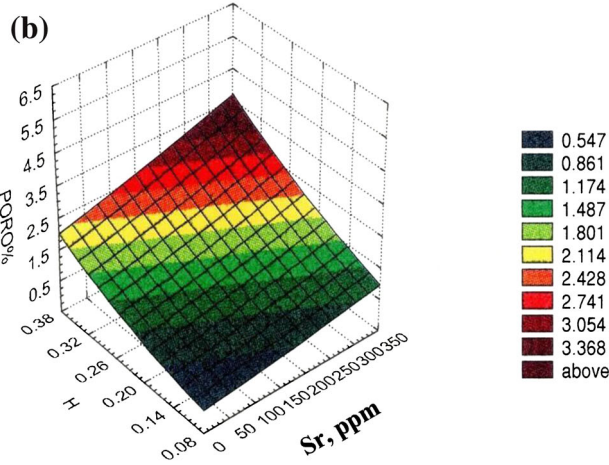
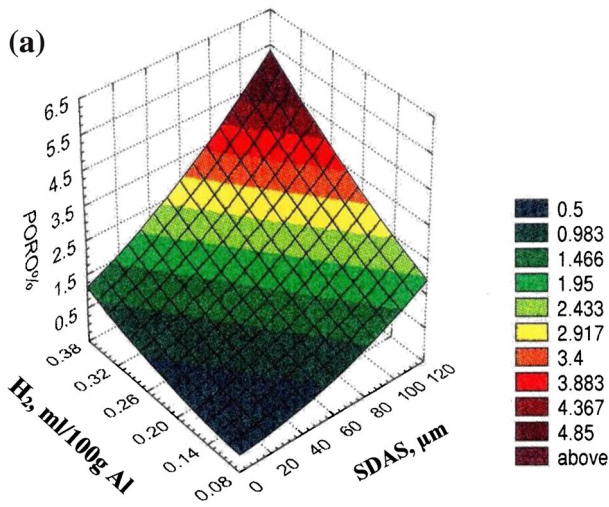


Figure 10. 3D surface plots obtained from directional solidification showing the effect of: (a) cooling rate, (b) Sr addition and (c) Ti addition.

regression designs (up to 300 variables) can be analyzed. Multiple response variables can be processed in pairs, and various options are available for counting missing data.

The independent variables (or controlling parameters) comprised the alloy parameters, viz. Si, Cu, Zn, Fe, Mg, Mn, Ti compositions, as well as the Sr and hydrogen (H) levels analyzed in each case, the grain refiner (GR) addition (taken as 0 or 0.02 %), the SDAS (μm), and the cooling time (TS-obtained from cooling curves) and solidus velocity (VS), giving a total of 13 variables.

Predictor terms (including interaction parameters) were constructed using these variables and tested for their ability to predict the response parameters (or dependent variables) of percentage porosity, average and maximum pore lengths/pore areas and the respective pore densities for both the exponential and irregular parts of the pore distribution curves in each case. Following these steps, data sets of 135 cases with 55 variables were obtained for the end-chill.

The two data sets were then explored using the StatSoft Statistica software program, until those predictor terms that gave the best possible fit to the data set were found. This was done by evaluating the R^2 value (that indicated the fraction of variance in the data set, an R^2 value of one representing a perfect correlation), the t value (which assessed the relative strength of each predictor term) and the p -level or significance number (which measured the relative significance of each term); the closer to zero the p -level, the more certain the relationship between the predictor term and the response parameter.

In the case of the end-chilled samples, good fits were obtained for almost all the response parameters, viz. for percentage porosity, and maximum pore area, average pore area, maximum pore length, and average pore length for the irregular part of the porosity distribution curves (i.e., big pores), with R^2 values ranging between 0.873 and 0.768. The maximum pore area showed the highest R^2 value (0.873), with percentage porosity (0.832) and average pore area (0.831) following closely. For all models, the predictor variables were H, SDAS, Sr, Ti and Mg, with cooling time (TS) and Cu as additional predictors in some of the models, like those for percentage porosity and average pore area.

Table 5 summarizes the predictor variables used to develop the various response surface models (response parameters), and the t values and significance levels obtained for each predictor in the respective cases. As can be seen, hydrogen is the parameter that has the greatest impact on the percentage porosity, followed by the SDAS, and then Sr, these parameters showing the highest t values and zero significance levels (the 0.00000 p -levels quoted in the table are actually 0.000000). However, as far as the other response parameters are concerned, i.e., those that correspond to the pore size (pore area/pore length), it is the SDAS that has the greater influence compared to hydrogen. The strongest impact of SDAS is on the

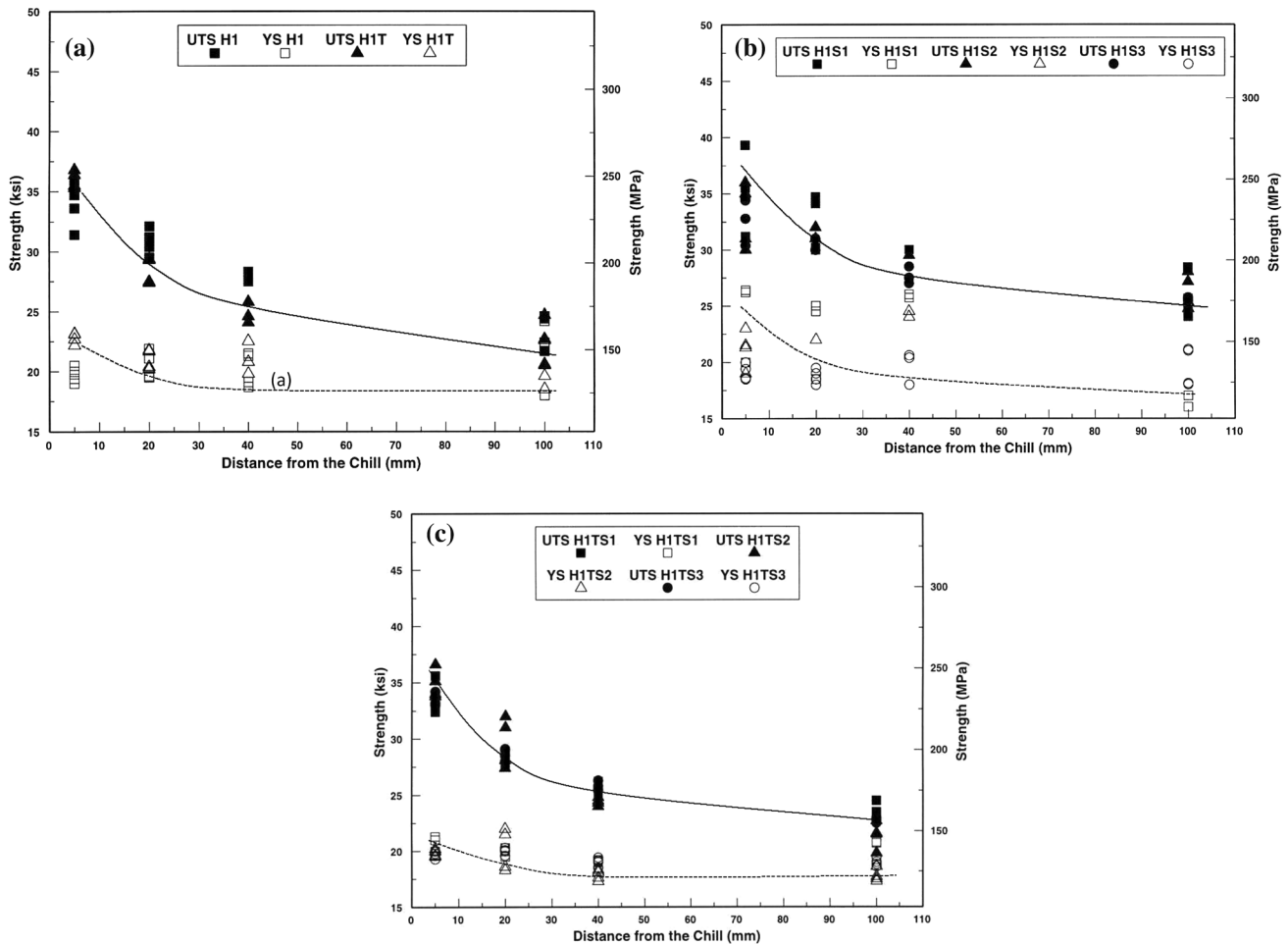


Figure 11. Variation in UTS and YS as a function of distance from the chill for (a) H1 and H1T alloys, (b) H1S alloys, (c) H1TS alloys.

maximum pore area, with a t value of 22.35 compared to 8.721 for hydrogen.

Comparing the effects of strontium and titanium (i.e., grain refiner) additions, strontium has the greater influence on the percentage porosity and pore areas (average and maximum). The pore lengths (average and maximum), however, are controlled more by titanium than by strontium. This is to be expected, in view of the effect that grain refiner addition has on reducing the grain size and, hence, the grain boundary facets along which the pores form, in other words, the pore lengths.

The above results strongly support our microstructural observations and qualitative analysis of porosity distribution reported earlier on in our work.¹⁰ Yet another interesting observation made from Table 5 is that Mg appears to have an influence comparable to that of hydrogen on the pore size response parameters of area and length. However, its overall effect on the percentage

porosity is much less compared to that of hydrogen, SDAS and strontium.

Figure 10a–c shows the 3D surface plots obtained from the end-chill directional solidification mold under different working conditions. For a given hydrogen level, decreasing the cooling rate (Figure 10a) leads to a remarkable increase in percentage of porosity. Addition of Sr up to 350 ppm also contributes to porosity formation but to a lesser extent compared to that obtained from cooling rate (Figure 10b). Grain refining using TiB₂ is the only parameter that would reduce the percentage porosity (Figure 10c).

Tensile Properties and Fractography

Figure 11a depicts the variation in UTS and YS for H1 and H1T alloys (hydrogen level ~0.1 ml/100 g Al) as a function of distance from the chill. The UTS is inversely

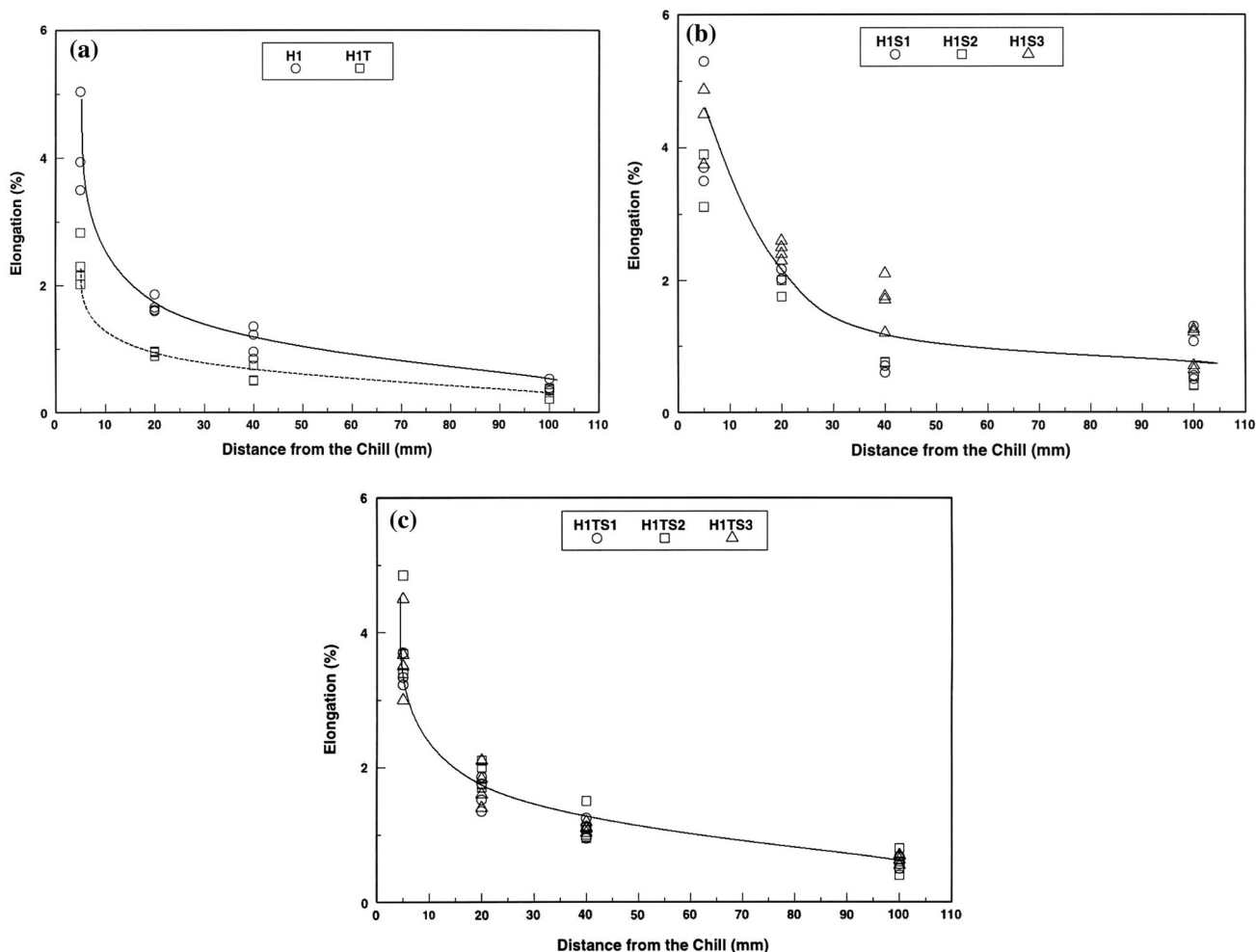


Figure 12. Variation in EL % as a function of distance from the chill for (a) H1 and H1T alloys, (b) H1S alloys, (c) H1TS alloys.

proportional to SDAS (represented by distance from the chill end). The relationships for both alloys, however, are nonlinear. It is also noted that at high cooling rates, grain-refined H1T alloy is somewhat superior to the non-grain-refined H1 alloy. As the cooling rate decreases, the difference in UTS becomes marginal. The values of YS are not affected much by the SDAS. The grain-refined alloy still offers a better strength compared to H1 alloy.

Figure 11b demonstrates the effect of Sr modification on UTS and YS levels with the increase in SDAS. It is seen that the addition of 300 ppm Sr leads to lower strengths compared to 100 ppm Sr, due to porosity formation as described earlier. It is worth noting here that the YS values for the modified alloys are higher compared to those for the unmodified alloys shown in Figure 11a. The general trend exhibited by both UTS and YS, however, is similar to that exhibited by the base H1 alloy. The yield and tensile strengths obtained from the modified, grain-refined alloys are shown in Figure 11c. While these values are comparable with those obtained from the grain-refined castings,

they are still lower than those obtained for the modified ones.

The ductility values of grain-refined as opposed to non-grain-refined alloys are shown in Figure 12a. As can be seen, the scattering in the data obtained from the non-grain-refined alloy is more, compared to the grain-refined case. Unexpectedly, however, the H1T alloy yielded ductility values inferior to those offered by H1 alloy. This result may be attributed to the increase in porosity due to the presence of the TiB_2 grain refining particles in H1T alloy, which provide nucleation sites for the porosity. The effect of Sr in negating this grain refining effect is highlighted by the higher strength values exhibited by the modified castings described above. It is also evident from Figure 12b that modification has a better impact on improving the alloy ductility than grain refining. The combined effect of grain refining and modification on the ductility of 319 castings is displayed in Figure 12c. The main observation is the consistence of the data as opposed to that shown in Figure 12a. In general, the results are seen to lie in between those for H1 and H1S alloys.

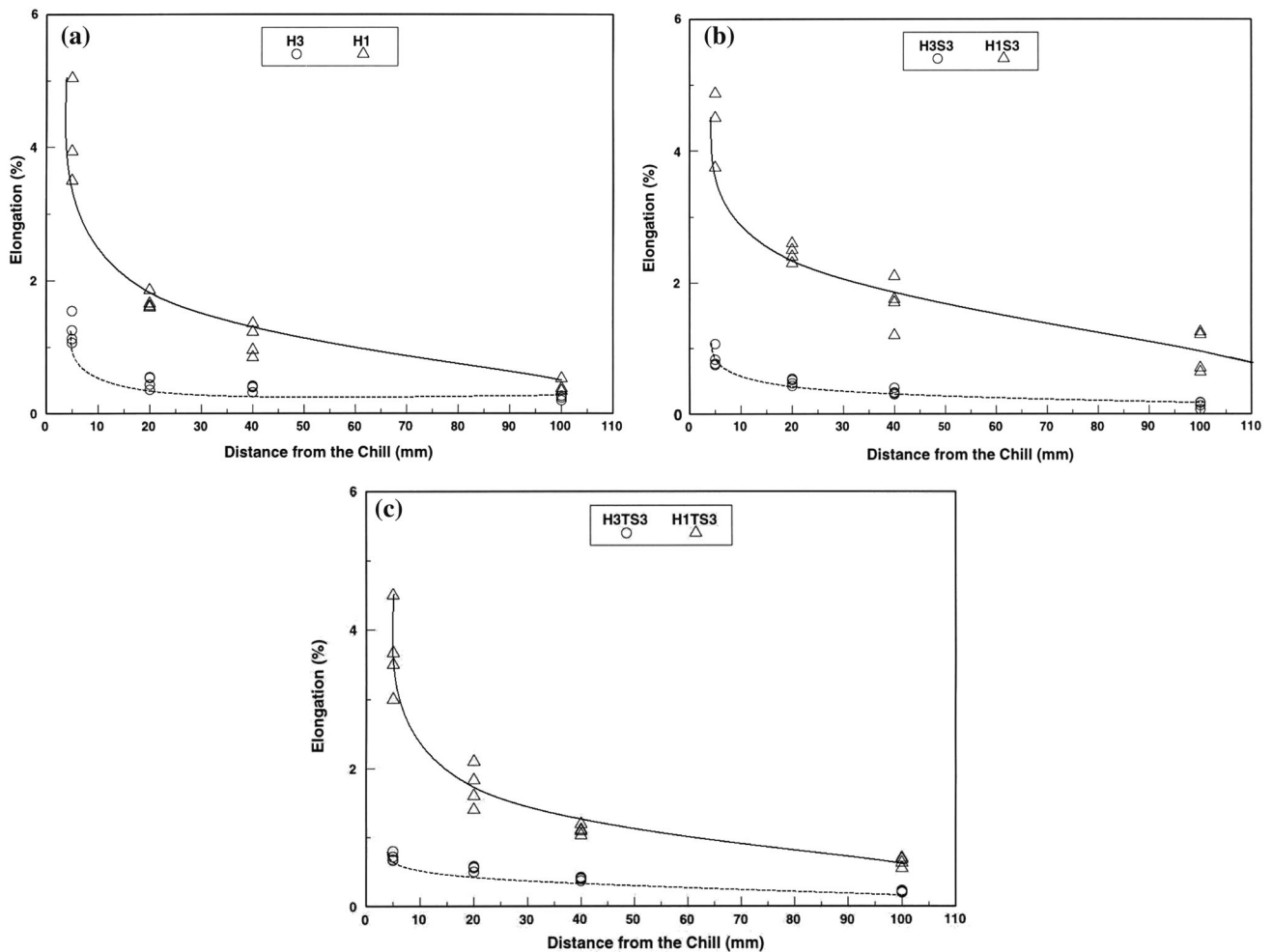


Figure 13. Variation in EL % as a function of distance from the chill for (a) H3 and H1 alloys, (b) H3S3 and H1S3 alloys, (c) H3TS3 and H1TS3 alloys.

Aluminum alloy melts are characterized by their high affinity for hydrogen absorption during melting and holding. During solidification, the hydrogen is rejected, resulting in the formation of porosity that significantly deteriorates the mechanical properties. An example of the deleterious effect of gas content is shown in Figure 13a. Addition of Sr in the presence of hydrogen (H3S3 alloy) increases the amount of porosity even at the highest cooling rate (i.e., at 5-mm distance from the chill end), leading to a further drop in ductility, as shown in Figure 13b. Introduction of grain refiner (H3TS3 alloy) apparently does not cause noticeable changes, as shown in Figure 13c. The relationships between the amount of porosity and alloy ductility for the various series are summarized in Table 6. The correlation of tensile properties with porosity in A319.2 alloy for all the melt treatment conditions studied is summarized in Figure 14, where the ductility–porosity relations show the significant influence of porosity on this property.

The purpose of fractography in the present work is to analyze features and attempt to relate the topography of

the fracture surface to the causes and/or basic mechanisms of fracture.²⁶ The knowledge of fracture behavior is important in upgrading material specifications, improving product design and analyzing failures for improved reliability.²¹

Figure 15a shows a general view of the fracture surface obtained from H1 alloy (100 mm level). Fine scattered porosities can be observed (black arrows). The high-magnification image in Figure 15b reveals that the crack takes place through the fracture of long brittle Si particles. The effect of modification of a H1 alloy with Sr (H1S alloy) appears in the formation of dimple structure with less number of cleavages as clearly demonstrated in Figure 15c under same cooling conditions. This observation may be attributed to the change in Si particle morphology from acicular to fibrous.²⁶

According to Dighe et al.,²⁷ in commercial A356 alloy, the fracture path of tensile-tested specimens primarily goes through the largest silicon particles, which constitute less than 1 % of the overall population of silicon particles in the bulk

Table 6. Variation in Percentage Elongation (El. %) as a Function of Alloy Composition, Distance from the Chill End (mm) and Percent Porosity

Alloy	Distance from chill (mm)	El. %	Porosity (%)	Alloy	Distance from chill (mm)	El. %	Porosity (%)
H1	5	4.5 ± 0.5	0.014	H3	5	0.85	0.513
	20	1.7 ± 0.16	0.024		20	0.5	1.613
	40	1.1 ± 0.3	0.212		40	0.4	1.795
	100	0.41	0.505		100	0.13	2.495
H1T	5	4.5 ± 0.9	0.029	H3T	5	1.13	0.582
	20	2.5 ± 1.0	0.115		20	0.55	1.974
	40	1.1 ± 0.8	0.187		40	0.42	2.217
	100	0.85 ± 0.5	0.363		100	0.27	2.694
H1S3	5	3.8 ± 0.6	0.027	H3S3	5	1.25	0.892
	20	2.5	0.150		20	0.47	2.638
	40	1.5 ± 0.5	0.696		40	0.34	2.784
	100	1.0 ± 0.25	1.183		100	0.28	4.830
H1TS3	5	3.7 ± 0.8	0.031	H3TS3	5	0.72	1.187
	20	1.8 ± 0.3	0.214		20	0.55	2.970
	40	1.1 ± 0.1	0.347		40	0.4	3.226
	100	0.63 ± 0.2	0.715		100	0.26	3.642

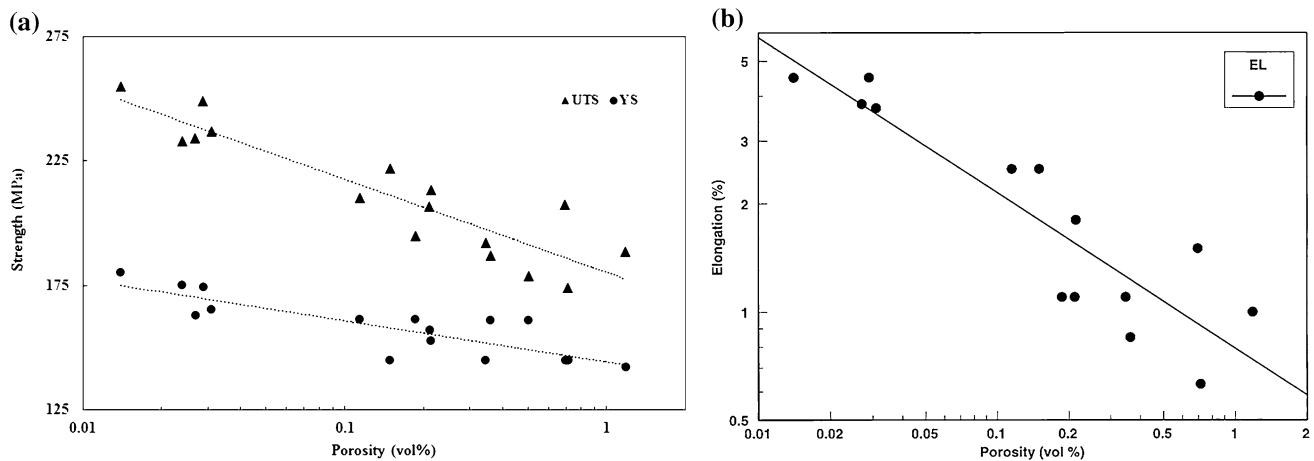


Figure 14. (a) Strength, and (b) percentage elongation versus percentage porosity relations in A319.2 alloy.

microstructure. Cáceres and Griffiths²⁸ have pointed out that, in Al-7Si-0.4 Mg casting alloys, the larger and longer silicon particles are more prone to cracking. In coarser structures, silicon particle cracking occurs at low strains, while in finer ones, the progression of damage is more gradual.

Increasing the hydrogen content from 0.1 to 0.2 ml/100 g (H2S1 alloy) resulted in the precipitation of relatively coarse pores compared to those obtained in the case of H1S1 alloy as shown in Figure 16. Figure 17a presents the fracture surface of a sample corresponding to H3S3 alloy. As can be seen, fairly large pores are formed near the sample edge and continue to the sample center. These pores, however, are disconnected (Figure 17b). Figure 17c

is a high-magnification fractograph showing the dendrite colonies inside the pores.

The effect of surface porosity on the fatigue life of PM390 hypereutectic Al-Si casting alloys was investigated by Ammar et al.^{8,14} at medium and elevated temperatures (150 and 300 °C). The author concluded from an analysis of the results obtained that surface porosity is the most critical casting defect which influences the fatigue life of hypereutectic alloys at medium and elevated temperatures. It was found that the most frequently observed fatigue crack initiation site was surface porosity where 89 % of all fatigue tested samples fractured as a result of this specific defect. Also, surface porosity has a detrimental effect on the

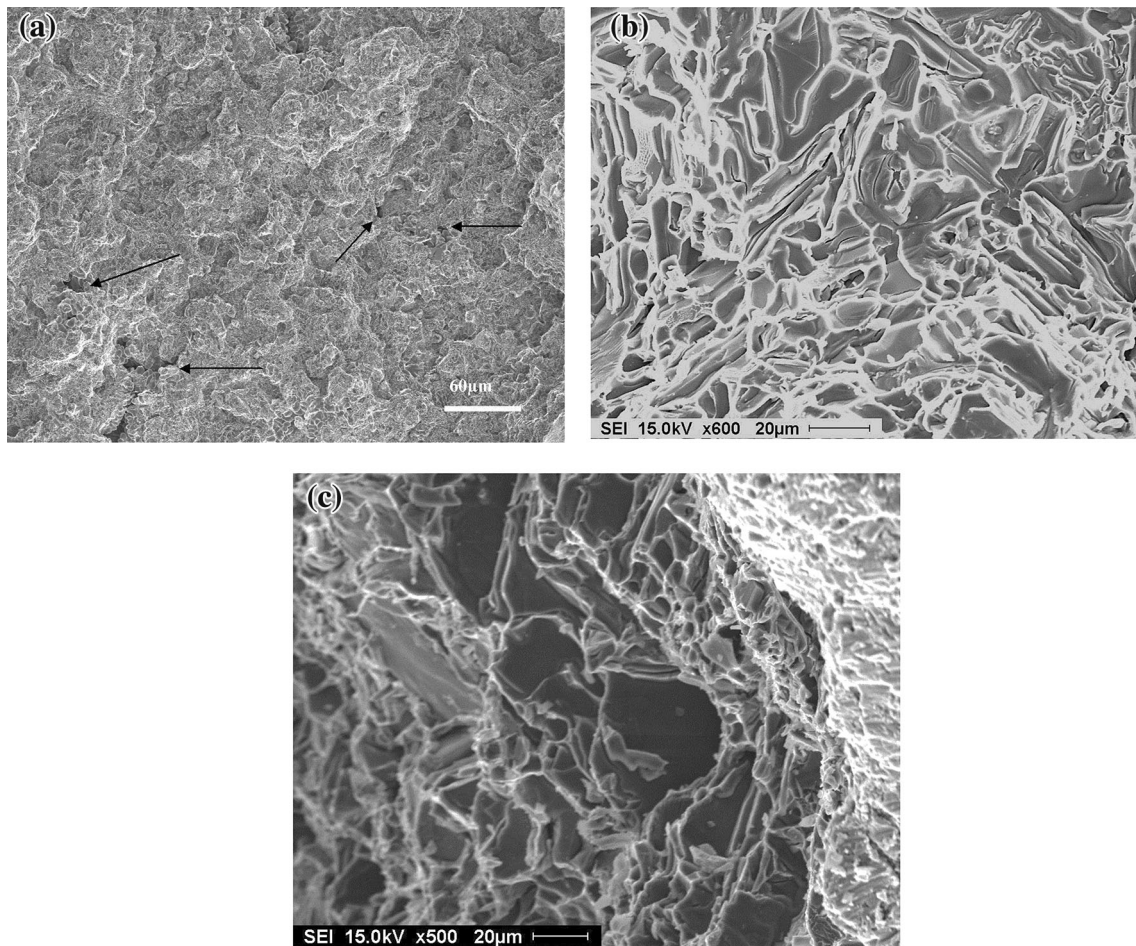


Figure 15. Fracture surface of samples sectioned at 100 mm above the chill: (a) H1 alloy—general view, (b) H1 alloy—high magnification showing the fracture of Si particles and (c) H1S alloy.

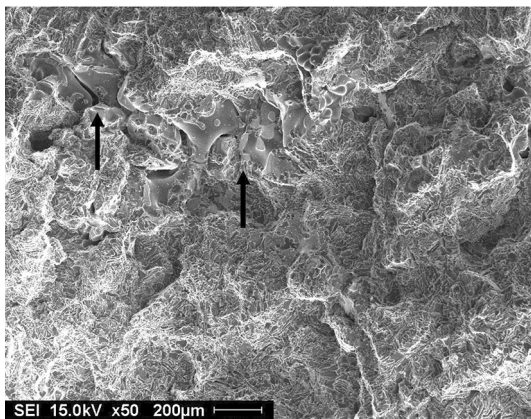


Figure 16. General view of the fracture surface of H2S1 alloy at 100 mm above the chill.

fatigue performance of the hypereutectic Al–Si casting alloy samples. It was observed that the fatigue strength decreases as the surface pore size increases and vice versa. The SEM technique may be applied with great accuracy for the measurement of single pores responsible for fatigue crack initiation.

Conclusions

Based on an analysis of the results obtained from the present study, the following points may be summarized.

1. With respect to cooling rate (obtained as a function of SDAS) as one parameter, the interaction effect of other parameters, namely hydrogen (H_2), modifier (Sr) and grain refiner (TiB_2) levels on the porosity, follows the order: $H_2 > Sr > TiB_2$.
2. At high cooling rates, pore nucleation takes place predominantly in intergranular regions. The pore morphology is mostly elongated, the pores being observed to lie along the grain boundaries (due to the long freezing range of the alloy). The probability of pore nucleation taking place in interdendritic regions increases at higher cooling rates, and the pore morphology tends to be more rounded, as well.
3. Although strontium addition increases the porosity, the beneficial effect of Sr modification (i.e., with respect to modification of the eutectic silicon

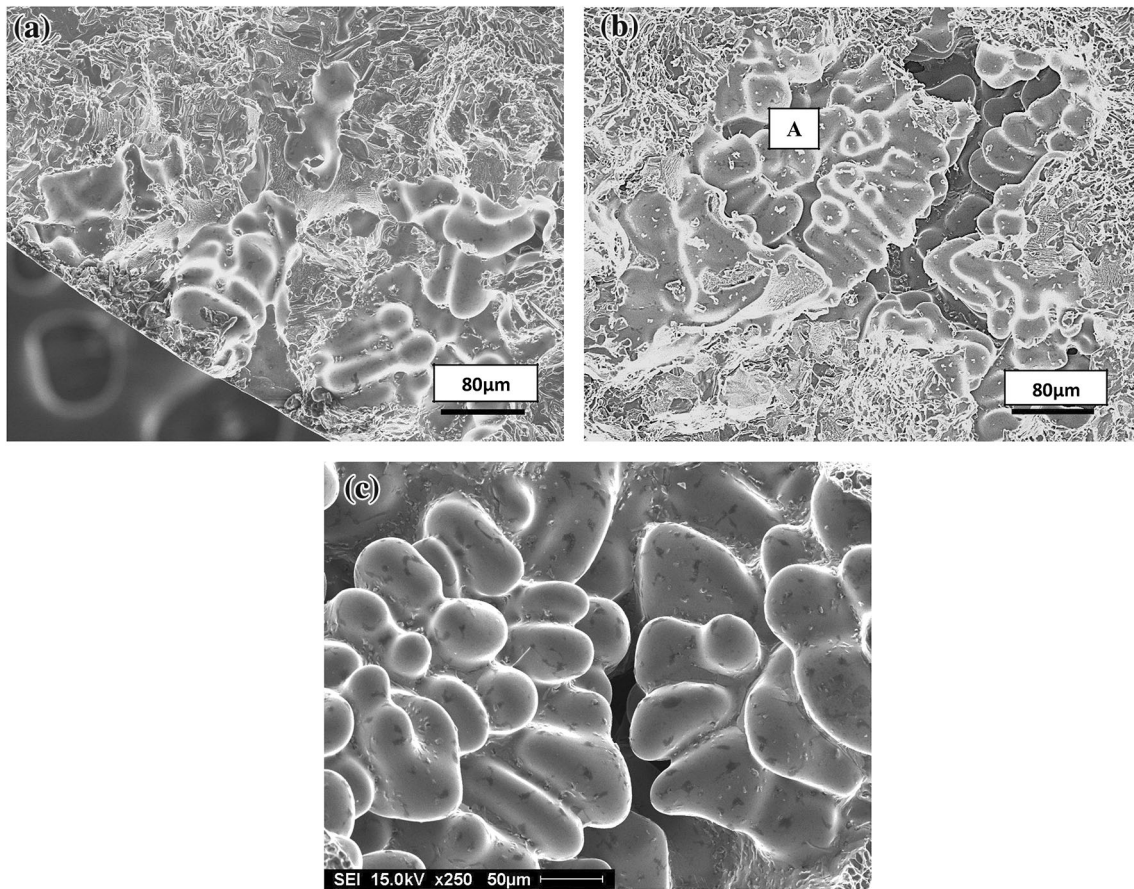


Figure 17. Fracture surface of a sample sectioned from H3S3 alloy at 100 mm above the chill: (a) area near the sample edge, (b) area near the sample center and (c) high magnification image of the area marked "A" in (b).

particles), however, improves the alloy ductility. Sr is also seen to poison the nucleation sites of the β - Al_5FeSi phase platelets observed in the alloy structure (these platelets act as active pore nucleation sites and are also detrimental to the alloy tensile properties).

4. Fragmentation and dissolution of the β -platelets takes place with increasing Sr levels, and the harmful effect of the iron intermetallic is greatly reduced. Comparisons of untreated, modified and grain-refined alloys show that the modified alloy contains the lowest amount of the iron phase.
5. Good fits for response parameters of percentage porosity, maximum pore area, average pore area, maximum pore length and average pore length are obtained from the statistical analysis of the porosity data for the end-chill mold samples. The results strongly support the microstructural observations/qualitative analysis of porosity formation in A319.2 alloy.
6. Hydrogen has the greatest influence on percentage porosity, followed by SDAS and Sr, for the end-chill mold samples. However, pore size is controlled more strongly by the SDAS than by

hydrogen, the strongest impact of SDAS being on the maximum pore area.

7. While percentage porosity and pore area are more influenced by strontium than by titanium (grain refiner) addition, pore length is controlled to a greater extent by the latter.
8. For the end-chill case, magnesium is also observed to have an influence comparable to that of hydrogen on the pore size (area/length).
9. The UTS is very sensitive to variations in the porosity and solidification conditions, and varies in a nonlinear fashion with respect to both. The YS is practically unaffected (in accordance with the literature). Ductility is also sensitive to variations in porosity and cooling rate, and follows a trend similar to that shown by the UTS.
10. Increasing the porosity volume fraction above 0.5 % in the base alloy (unmodified and non-grain-refined) reduces the ductility to negligible levels. Sr modification and grain refining allow for increases in the porosity level before the same level of degradation in ductility is observed.
11. Cooling rate (i.e. SDAS) significantly influences the ductility at low hydrogen levels. At higher levels,

however, hydrogen has a more pronounced effect (porosity related) on the drop in ductility.

12. Sensitivity of tensile properties to SDAS allows for the use of the latter as a good indicator of the expected tensile properties of the alloy.

Acknowledgments

The authors would like to thank Ms. Amal Samuel for enhancing the image/art work in the present article.

REFERENCES

1. R.J. Garino, S. Wakesberg, Automobile material choices. *Scrap Process. Recycl.* **51**, 101–105 (1994)
2. Z. Ma, *Effect of Fe-Intermetallics and Porosity on Tensile and Impact Properties of Al–Si–Cu and Al–Si–Mg Cast Alloys*, Ph.D. Thesis (Université du Québec à Chicoutimi, Canada, 2003)
3. A.M. Samuel, F.H. Samuel, H.W. Doty, Observations on the formation of β -Al₅FeSi phase in 319 type Al–Si alloys. *J. Mater. Sci.* **31**, 5529–5539 (1996)
4. J. Espinoza-Cuadra, P. Gallegos-Acevedo, H. Mancha-Molinar, A. Picado, Effect of Sr and solidification conditions on characteristics of intermetallic in Al–Si 319 industrial alloys. *Mater. Des.* **31**, 343–356 (2010)
5. L. Liu, A.M. Samuel, F.H. Samuel, H.W. Doty, S. Valtierra, Role of iron in relation to silicon modification in Sr-treated 319 and 356 alloys. *Int. J. Cast Met. Res.* **16**, 397–408 (2003)
6. L. Liu, A.M. Samuel, F.H. Samuel, H.W. Doty, S. Valtierra, Characteristics of alpha-dendritic and eutectic structures in Sr-treated Al–Si casting alloys. *J. Mater. Sci.* **39**, 215–224 (2004)
7. K. Tylenius, J.F. Major, D. Apelian, Optimization of castings parameters for production of sound Al castings: a response surface methodology approach. *AFS Trans.* **101**, 401–413 (1993)
8. H.R. Ammar, A.M. Samuel, F.H. Samuel, Effects of surface porosity on the fatigue strength of AE425 and PM390 hypereutectic Al–Si casting alloys at medium and elevated temperatures. *Mater. Sci. Eng. A* **473**, 58–64 (2008)
9. G.A. Edwards, G.K. Sigworth, C.H. Cáceres, D.H. St. John, J. Barresi, *Microporosity Formation in Al–Si–Cu–Mg Casting Alloys*, Paper to be presented at the 1997 AFS Casting Congress in Seattle
10. A.M. Samuel, F.H. Samuel, A metallographic study of porosity and fracture behavior in relation to the tensile properties in A319.2 end chill castings. *Metall. Mater. Trans. A* **26**, 2359–2372 (1995)
11. N. Roy, A.M. Samuel, F.H. Samuel, Porosity formation in Al–9 Wtpct Si–3 Wtpct Cu alloy systems: metallographic observations. *Metall. Mater. Trans. A* **27A**, 415–429 (1996)
12. C. Dupuis, Z. Wang, J.-P. Martin, C. Allard, in *Light Metals 1992*, ed. by E.R. Cutshall (The Minerals, Metals and Materials Society, 1992), pp. 1055–1068
13. D.L. McLellan, Tensile properties of A357-T6 aluminum castings. *J. Test. Eval.* **8**(4), 170–176 (1980)
14. H.R. Ammar, A.M. Samuel, F.H. Samuel, Porosity and the fatigue behavior of hypoeutectic and hypereutectic aluminum-silicon casting alloys. *Int. J. Fatigue* **30**, 1024–1035 (2008)
15. L. Liu, A.M.A. Mohamed, A.M. Samuel, F.H. Samuel, H.W. Doty, S. Valtierra, Precipitation of β -Al₅FeSi phase platelets in Al–Si based casting alloys. *Metall. Mater. Trans. A* **40**, 2457–2469 (2009)
16. Z. Ma, A.M. Samuel, F.H. Samuel, H.W. Doty, S. Valtierra, A study of tensile properties in Al–Si–Cu and Al–Si–Mg alloys: effect of β -iron intermetallics and porosity. *Mater. Sci. Eng. A* **490**, 36–51 (2008)
17. Z. Ma, E. Samuel, A.M.A. Mohamed, A.M. Samuel, F.H. Samuel, H.W. Doty, Parameters controlling the microstructure of Al–11Si–2.5Cu–Mg alloys. *Mater. Des.* **31**, 902–912 (2010)
18. N. Roy, M. Eng. Thesis (UQAC, Chicoutimi, 1995)
19. E. Samuel, B. Golbahar, A.M. Samuel, H.W. Doty, S. Valtierra, F.H. Samuel, Effect of grain refiner on the tensile and impact properties of Al–Si–Mg cast alloys. *Mater. Des.* **56**, 468–479 (2014)
20. Y. Han, A.M. Samuel, H.W. Doty, S. Valtierra, F.H. Samuel, Optimizing the tensile properties of Al–Si–Cu–Mg 319-type alloys: role of solution heat treatment. *Mater. Des.* **58**, 426–438 (2014)
21. Z. Ma, A.M. Samuel, H.W. Doty, S. Valtierra, F.H. Samuel, Effect of Fe content on the fracture behaviour of Al–Si–Cu cast alloys. *Mater. Des.* **57**, 366–373 (2014)
22. A.M. Samuel, H.W. Doty, S. Valtierra, F.H. Samuel, Effect of grain refining and Sr-modification interactions on the impact toughness of Al–Si–Mg cast alloys. *Mater. Des.* **56**, 264–273 (2014)
23. N. Roy, P.R. Louchez, F.H. Samuel, Statistical analysis of porosity in Al–9 wt% Si–3 wt% Cu–X alloy systems. *J. Mater. Sci.* **31**, 4725–4740 (1996)
24. G.E.P. Box, W.G. Hunter, J.S. Hunter, *Statistics for Experimenters* (Wiley, New York, 1978)
25. L. Davies, *Efficiency in Research, Development and Production: The Statistical Design and Analysis of Chemical Experiments* (The Royal Society of Chemistry, Cambridge, 1993)
26. G. Casella, *Statistical Design: Principles, Recommendations and Opinions*, Special Report (University of Florida, 2008)
27. M.D. Dighe, A.M. Gokhale, M.F. Horstemeyer, Effect of loading condition and stress state on damage evolution of silicon particles in an Al–Si–Mg–Base cast alloy. *Metall. Mater. Trans. A* **33A**(3), 555–565 (2002)
28. C.H. Cáceres, J.R. Griffiths, Damage by the cracking of Si particles in an Al–7Si–0.4Mg casting alloy. *Acta Mater.* **44**, 15–23 (1996)